The 14th International Topical Meeting on Nuclear Reactor Thermalhydraulics, NURETH-14
Toronto, Ontario, Canada, September 25-30, 2011

NURETH14-240

TWO-DIMENSIONAL SIMULATION OF THE DOWNCOMER BOILING EXPERIMENT USING THE CUPID CODE

A. Hyoung Kyu Cho[1], B Byong Jo Yun[1], C. Jae Ryong Lee[1], D. Han Young Yoon[1], E. Jae Jun Jeong[2,*]

[1] Korea Atomic Energy Research Institute, Daejeon, Korea
[2] Pusan National University, Busan, Korea

hkcho@kaeri.re.kr, bjyun@kaeri.re.kr, jrlee@kaeri.re.kr, hyyoon@kaeri.re.kr,
[*] jjjeong@pusan.ac.kr

Abstract

For the analysis of transient two-phase flows in nuclear reactor components, a three-dimensional thermal hydraulics code, named CUPID, has been being developed. We simulated the DOBO (Downcomer Boiling) experiment in two-dimensions using the CUPID code to evaluate its two-phase flow models and verify its applicability to the downcomer boiling analysis. The simulation result showed that it can reproduce the important characteristics of the downcomer boiling, such as a flow pattern change and a circulation of liquid accelerated by bubbles. The two-phase flow models that require further improvement were identified as well for an enhanced prediction of the downcomer boiling.

1. Introduction

The need for a multi-dimensional analysis of the thermal hydraulic phenomena in a component of a nuclear reactor is increasing with the advanced design features, such as a direct vessel injection system, a gravity-driven safety injection system, and a passive secondary cooling system. In an advanced pressurized water reactor, multi-dimensional phenomena inside the reactor vessel during a postulated loss of coolant accident have become major technical issues for consideration [1]. These include the ECC (Emergency Core Coolant) bypass of a DVI (Direct Vessel Injection) system and a downcomer boiling during the LBLOCA (Large Break Loss of Coolant Accident) reflood phase. These phenomena are characterized by the combination of a boiling due to a downcomer wall heat transfer, multi-dimensional counter-current flow, lateral motion of bubbles and droplets, flow regime change, bulk condensation, phase separation, etc. These features require more detailed analysis with enhanced accuracy because of the complicated multi-dimensional effects. Motivated by these issues, the development of a numerical solver for a multi-dimensional thermal hydraulic analysis code, named CUPID [2], is in progress at KAERI (Korea Atomic Energy Research Institute). The objective of the development is to support a resolution for the thermal hydraulic issues regarding the transient multi-dimensional two-phase flow which can arise in a component of an advanced light water reactor.

[*] Corresponding author

The numerical solver and two-phase flow models of the CUPID code have been established as a standalone code. They have been validated against various conceptual problems and thermal-hydraulic experiments in our previous studies [3,4,5] and the assessment strategy for the future verification and validation was outlined in Jeong et al [2]. In addition to these, the coupling with a system analysis code, MARS [6] and a three-dimensional kinetics code, MASTER [7] has been completed recently, which is expected to provide the advanced multi-scale and multi-physics calculations for many safety related issues of the light water reactors [8]. The verification results for the coupled calculation showed that the multi-scale and multi-physics calculation using the CUPID code can be one of the major applications of the code in the future.

As a multi-scale application, it is being considered to use the CUPID code, coupled with MARS, for the simulation of the downcomer boiling phenomena. They were known to happen in the downcomer of a nuclear reactor vessel during the reflood phase of a postulated loss of coolant accident [9]. The stored energy release from the reactor vessel to the emergency core coolant inside the downcomer causes the boiling on the wall, and it can reduce the hydraulic head of the accumulated water, which is the driving force of water reflooding to the reactor core. These phenomena have been considered as a technical issue of an advanced light water reactor because it is concerned with the core cooling capability of a safety injection system. Due to the large hydraulic diameter of the downcomer and the low velocity of the downward liquid, it was reported that the boiling phenomena have an apparent multi-dimensional behavior; for example, the swirling of the liquid flow in the downcomer, which is not able to be reproduced by the one-dimensional approach [9]. In this attempt to analyze this phenomena in a multi-scale frame, the CUPID code has been proposed to simulate the downcomer region of the reactor vessel where the multi-dimensional boiling phenomena is important while the MARS code does the remaining parts of the reactor vessel. Prior to this coupled simulation for the downcomer boiling, it is required to validate the CUPID code and its two-phase flow models against available downcomer boiling data. For this purpose, in this study, the downcomer boiling experiment (DOBO) was simulated using the CUPID code as a stand-alone code, which was performed at KAERI to understand the boiling inside the downcomer and provide the data for the code validation.

The purpose of this study is to validate the two-phase flow models of the CUPID code for the analysis of downcomer boiling. The reproduction of the important characteristics of the boiling phenomena in a large duct using the code was of special interest. In this paper, the physical models and correlations of the code were described in detail and the numerical simulation result were compared to the DOBO experiment.

2. Two-Phase Flow Models

In the two-fluid model for the two-phase flow analysis, the mass, energy, and momentum equations for each field are established separately, and then, they are linked by the interfacial mass, momentum, and energy transfer models. For a mathematical closure, the constitutive relations for the interfacial drag force, the interfacial heat transfer and the wall heat partitioning are necessary and these are summarized in this chapter.

2.1 Inter-phase topology map

In a two-fluid model, the mass, momentum and energy transfers between phases depend on the shape of their interfaces and the conventional system and component analysis codes use flow regime maps. The traditional flow regime concept, however, is not applicable to open medium analyses because, in the traditional concept, every cell needs to include a wall boundary for the cross sectional average of a flow parameter. To address this issue, CFD-BWR code [10], built on the foundation of STAR-CD [11], proposed an inter-phase surface topology map recently. In their works, simulations have been conducted not only for dispersed flows but also for flows involving a local sharp interface such as slug and annular mist flows. According to their approach, the three main types of local inter-phase surface topologies and the transitional regions are distinguished. Three main topologies are a bubbly flow topology, a mist flow topology and a sharp interface topology as shown in Figure 1. The transitional topologies are the overlapping regions of two or three main topologies. The topology in each mesh cell is determined by two parameters, a void fraction (α_g) and a gradient of the void fraction ($\gamma = \delta \cdot |\nabla \alpha_g|$). Tentner et al. [12, 13], Ioilev et al. [14] and Ustinenko et al. [15] have established a significant progress to verify and validate this approach. The inter-phase topology concept proposed by Tentner et al. [12] was employed to the present numerical solver in order to deal with the flow pattern change from the bubbly flow to the churn or annular flow.

The transition criteria of the void fraction and the void fraction difference and the definition of the characteristic length (δ) are

$$\alpha_{g,bc} = 0.3,\ \ \alpha_{g,cm} = 0.95,\ \ \gamma_1 = 0.2\ \text{ and }\ \gamma_2 = 0.4, \tag{1}$$

where $\gamma = 0.5 \cdot \vec{\delta} \cdot \left[\left| \frac{\partial \alpha_g}{\partial x} \right| \mathbf{i} + \left| \frac{\partial \alpha_g}{\partial y} \right| \mathbf{j} + \left| \frac{\partial \alpha_g}{\partial z} \right| \mathbf{k} \right]$ and $\vec{\delta} = \frac{V_i}{\sum_f |S_{f,x}| / N_f} \mathbf{i} + \frac{V_i}{\sum_f |S_{f,y}| / N_f} \mathbf{j} + \frac{V_i}{\sum_f |S_{f,z}| / N_f} \mathbf{k}$.

Once a local topology is determined for each cell, the interfacial area and interfacial transfer models, thereafter, are defined depending on the topology of the cell.

2.2 Interfacial area concentration

The interfacial area concentration models for the present calculation are summarized in Table 1.

2.3 Interfacial momentum transfer

The interfacial momentum transfer term, $\underline{M}_{ik}$ includes the interfacial drag, the momentum exchange due to the phase change at the interface and wall, and various non-drag forces such as the virtual mass force, lift force, wall lubrication force and turbulent dispersion force. $\underline{M}_{ik}$ is written as:

$$\underline{M}_{ig} = -\underline{F}_{gl} + \Gamma_v \underline{u}_{gi} + \Gamma_{wall} \underline{u}_{gi} + \underline{F}_{nd} = -\underline{M}_{il} \,. \tag{2}$$

The interfacial drag force terms in the momentum equations can be expressed as;
for dispersed topology,

$$\underline{F}_{gl} = \frac{1}{8} A_i \rho_c C_D \,|\, \underline{u}_g - \underline{u}_l \,|\, (\underline{u}_g - \underline{u}_l) \quad , \tag{3}$$

for interface topology,

$$\underline{F}_{gl} = \frac{1}{2} A_i \rho_g C_i(\varphi) \,|\, \underline{u}_g - \underline{u}_l \,|\, (\underline{u}_g - \underline{u}_l) \,. \tag{4}$$

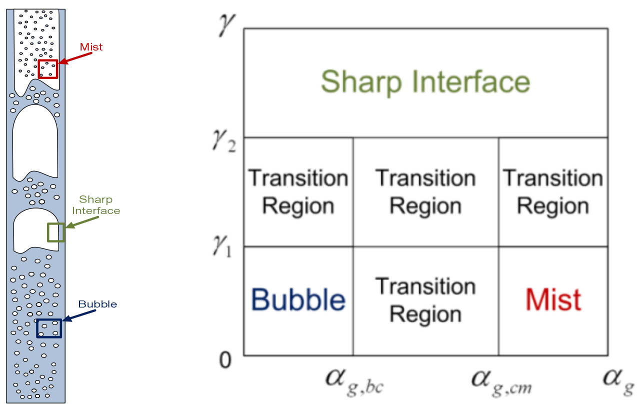

Figure 1 Inter-phase surface topology concept [12]

Table 1 Interfacial area concentration models for CUPID

Topology	Interfacial Area Correlations
Bubble [16]	$A_i = \frac{6\alpha_g}{D_b}$, $\quad D_b = 4.34 \cdot Lo \cdot N_{Lo}^{-0.335} \cdot \alpha^{0.170} \cdot \mathrm{Re}_b^{-0.239}$, where, $N_{Lo} = \frac{Lo}{D_H}$, $\mathrm{Re}_b = \frac{\varepsilon^{1/3} Lo^{4/3}}{\nu_f}$, $Lo = \sqrt{\frac{\sigma}{g\Delta\rho}}$, $\varepsilon = g \,\|\, j_g \,\|\, \exp(-0.0005839\,\mathrm{Re}_f) + \frac{\|j\|}{\rho_m}\left(-\frac{dp}{dz}\right)_F \{1-\exp(-0.0005839)\mathrm{Re}_f\}$, $\mathrm{Re}_f = \frac{j_f D_H}{\nu_f}$ and $\left(-\frac{dp}{dz}\right)_F$ is the frictional pressure drop calculated with Lockhart–Martinelli's correlation [17].
Drop [18]	$A_i = \frac{6(1-\alpha_g)}{D_d}$, $\quad D_d(P,\alpha_g) = 0.01 \frac{\sigma}{\rho_g j_g^2} \mathrm{Re}_g^{2/3} \left(\frac{\rho_g}{\rho_f}\right)^{-1/3} \left(\frac{\mu_g}{\mu_f}\right)^{2/3}$.
Interface [19]	$A_i = \|\nabla \alpha_g\|$.

The interfacial drag force in the transition topology was calculated from the linear interpolation between the values of two different topologies. Interfacial drag coefficients C_D and $C_i(\varphi)$ used in the present calculation are listed in Table 2.

The current CUPID code has four non-drag forces; the virtual mass force, lift force, wall lubrication force and turbulent dispersion force,

$$\underline{F}_{nd} = \underline{F}_{vm} + \underline{F}_{lift} + \underline{F}_{wl} + \underline{F}_{td} . \quad (5)$$

The virtual mass force was applied for all topologies and the other forces were considered when either bubble topology or churn topology was identified. The definitions of each term and the implemented models for these are presented in Table 3.

2.4 Interfacial mass and heat transfer

The interfacial mass and heat transfer terms are written as;

$$Q_{ig} = P_s / P \cdot H_{ig} A_i (T_{sat} - T_g) + \Gamma_v h_{gi} + \Gamma_{wall} h_{g,sat} , \quad (6)$$

$$Q_{il} = H_{il} A_i (T_{sat} - T_l) - \Gamma_v h_{li} - \Gamma_{wall} h_l , \quad (7)$$

$$\Gamma_v = - \frac{\frac{P_s}{P} H_{ig} A_i (T_{sat} - T_g) + H_{il} A_i (T_{sat} - T_l)}{h_{gi} - h_{li}} . \quad (8)$$

where $(h_{gi}, h_{li}) = (h_{g,sat}, h_l)$ if $\Gamma \geq 0$ and $(h_{gi}, h_{li}) = (h_g, h_{l,sat})$ if $\Gamma < 0$. The interfacial heat transfer coefficients for the dispersed topologies adopted for the present solver are Ranz and Marshall correlation [20] and that for the interfacial topology is shown in Eq. (9) [12].

$$H_{ik} = St \rho_k c_{p,k} \,|\, \underline{u}_{g\tau} - \underline{u}_{l\tau} \,| , \quad (9)$$

where $St = 0.0045 \left(\rho_g \,|\, \underline{u}_g \,|\, \mu_l / \rho_l \,|\, \underline{u}_l \,|\, \mu_g \right)^{1/3}$ and $\underline{u}_{g\tau} - \underline{u}_{l\tau} = \left(\underline{u}_g - \underline{u}_l \right) - \left[\left(\underline{u}_g - \underline{u}_l \right) \cdot \frac{\nabla \alpha}{|\nabla \alpha|} \right] \frac{\nabla \alpha}{|\nabla \alpha|}$.

Table 2 Interfacial drag coefficient models for CUPID

Topology	Interfacial Drag Coefficients
Bubble and drop [12]	$C_x = \frac{24}{\mathrm{Re}_x} \left(1 + 0.15 \,\mathrm{Re}_x^{0.687} \right)$ for $0 < \mathrm{Re}_x \leq 1000$, $C_x = 0.44$ for $\mathrm{Re}_x > 1000$ and $x = b \, or \, d$
Interface [12]	$C_i(\varphi) = C_{i,\tan} + (C_{i,ort} - C_{i,\tan}) \,|\cos\varphi|$, where $C_{i,\tan} = 0.005$ and $C_{i,ort} = 1$, $\cos\varphi = \frac{(\underline{u}_g - \underline{u}_l) \cdot \nabla \alpha}{\left| (\underline{u}_g - \underline{u}_l) \right| \,|\nabla \alpha|}$.
Interpolation Region	$\underline{F}_{gl} = \chi_i (\underline{u}_g - \underline{u}_l)$, $\left(\chi_i \right)_{transition} = w \cdot \left(\chi_i \right)_1 + (1 - w) \cdot \left(\chi_i \right)_2$, where $w = \frac{\alpha_{g,cm} - \alpha_g}{\alpha_{g,cm} - \alpha_{g,bc}}$ or $w = \frac{\gamma_2 - \gamma}{\gamma_2 - \gamma_1}$.

Table 3 Interfacial non-drag force models for CUPID

	Non-drag Interfacial Force Models
Virtual mass force [21]	$\underline{F}_{vm,g} = C_g^{vm}\alpha_g\alpha_l\rho_m \frac{\partial(\underline{u}_l - \underline{u}_g)}{\partial t} = -\underline{F}_{vm,l}$, where $\rho_m = (\alpha_g\rho_g + \alpha_l\rho_l)$, $C_g^{vm} = \frac{(1+2\alpha_g)}{2(1-\alpha_g)}$ if $\alpha_g < 0.5$, $C_g^{vm} = \frac{(3-2\alpha_g)}{2\alpha_g}$ otherwise.
Lift force [22]	$\underline{F}_{lift,g} = \alpha_g\rho_l C_{lift}(\underline{u}_g - \underline{u}_l)\otimes(\vec{\nabla}\otimes\underline{u}_l) = -\underline{F}_{lift,l}$, where $C_L = \begin{vmatrix} \min[0.288\tanh(0.121\,\mathrm{Re}_b), f(E_{o,H})], \; if \; E_o < 4 \\ f(E_{o,H}), \; if \; 4 \le E_o < 10 \\ -0.27, \quad if \; 10 \le E_o \end{vmatrix}$, $\mathrm{Re}_b = \frac{\rho_l\lvert\underline{u}_g - \underline{u}_l\rvert D_b}{\mu_l}$, $f = 0.00105E_{o,H}^3 - 0.0159E_{o,H}^2 - 0.0204E_{o,H} + 0.474$, $E_{o,H} = \frac{g(\rho_l - \rho_g)d_H^2}{\sigma}$, $d_H = D_b\left(1 + 0.163E_o^{0.757}\right)^{1/3}$, $E_o = \frac{g(\rho_l - \rho_g)D_b^2}{\sigma}$.
Wall lubrication force [23]	$\underline{F}_{wl} = \frac{-\alpha_g\rho_l C_{wl}\lvert\underline{u}_g - \underline{u}_l\rvert^2}{D_b}\max\left(0, C_1 + C_2\frac{D_b}{y_{wall}}\right)\vec{n}$, where $C_1 = -0.01$, $C_2 = 0.05$.
Turbulent dispersion force	$\underline{F}_{td} = -C_{TD}\rho_l k_l \nabla\alpha_l$, where $C_{TD} = 0.1$.

During flashing, where $T_l > T_{sat}$, the liquid-side heat transfer factor is calculated using the following approximate model:

$$H_{il}A_i = \max(10^6, H_{il}A_i) . \tag{10}$$

A superheated liquid quickly returns back to its saturated condition by this model. The value, 10^6 was referred to in [24].

The wall boiling on a heated surface is simulated by a wall heat flux partitioning model. In this model, the mechanisms of a heat transfer from the wall to a two-phase flow consist of the surface quenching (q_q), evaporation (q_e) and single phase convections (q_{wlc} and q_{wgc}). The wall-to-liquid heat transfer (q_{wl}) is the sum of the q_q and q_{wlc} . It is assumed that the direct contact heat transfer between droplets and the wall is negligible so that a gas phase convective heat transfer is merely considered for the mist topology ($q_{wgc} = q_{wg}$) . Then, an equation of the heat flux conservation on a heated surface is

$$q_{wall} = \frac{\alpha_{g,cm} - \alpha_g}{\alpha_{g,cm} - \alpha_{g,bc}}\left(q_q + q_e + q_{wlc}\right) + \frac{\alpha_g - \alpha_{g,bc}}{\alpha_{g,cm} - \alpha_{g,bc}} q_{wg} . \tag{11}$$

The closure relations for this heat flux partitioning were listed in Bae [25].

2.5 Turbulence modelling

In the CUPID, two models are available for the turbulent shear stress; one is the mixing length model and the other one is the *k-ε* model. In the present study, the mixing length model was used with the bubble induced turbulence terms, which were proposed by Michiyochi and Serizawa [26] because the two-phase flow induced turbulent terms has not been modelled for the *k-ε* model of CUPID in a churn or annular flow region. The enhancement of the *k-ε* model for the high void fraction condition is in progress. Meanwhile, in a two-phase flow, it was reported that the existence of bubbles on the wall boundary layer has a significant influence on the velocity profile nearby the wall. To account for this effect, the two-phase wall function proposed by Yun et al. [27], was implemented for the boiling flow simulation.

3. DOBO facility and test result

The DOBO test facility was designed to simulate the downcomer boiling phenomena that may occur in the lower downcomer region below a cold leg during the reflood phase of a postulated LBLOCA [9]. The DOBO facility consists of a test section, a steam–water separator, a condenser, a heat exchanger, a drain pump, a storage tank, an air injection and ventilation system, a pre-heater and an injection pump, as shown in Figure 2-(a). Among these, the test section was simulated by the CUPID code for the present calculation. It has rectangular duct geometry and its dimensions are 6.4 m high, 0.25 m wide and 0.30 m deep. The height and width are the same with the APR1400 downcomer, but the circumference is reduced to 47.08-fold. One among four side walls of the test section incorporates 207 cartridge heaters inside it to simulate the stored energy release from the reactor vessel wall. The heated region starts 0.3 m above the inlet, and ends 1.0 m below the outlet. Figure 2-(b) indicates the schematic diagram of the test section. The DOBO test was performed with four different heat fluxes and among them, DOBO-R2-1 test case conducted with 70.8 kW/m^2 was selected for the current simulation because it is the closest value to the predicted heat flux of the reflood phase.

In an accident condition, the emergency core cooling water flows down into the downcomer from the elevation of the ECC injection nozzle to the lower plenum. Thus, the downcomer boiling happens with the downward liquid flow, and then the counter-current flow appears between the liquid and upward bubbles near the reactor vessel wall. The liquid inlet, therefore, was located at the upper region of the test section as indicated in Figure 2-(b). The injected liquid impinges on the test section wall and flows downward forming a liquid film. The inlet flow rate was 1.33 kg/s in DOBO-R2-1 test. Due to the heat released from the heated wall, boiling occurs in the test section. The generated steam flows out from the test section through the outlet, where the pressure was maintained at 1.6 bars. The accumulated liquid formed a free surface inside the channel and the water level was maintained at 5.4 m by controlling the liquid outlet flow rate located at the bottom of the test section.

The major measuring parameters of the DOBO test are the void fraction, gas velocity, liquid velocity, water temperature and pressure along the elevation. The details of the measurement instrumentations and the results were reported in Yun et al. [9]. Figure 3-(a) shows the experimental results of the local void fraction measured with five-conductance probes. The void fraction distributions at the elevations, 1.53 m and 2.53 m, indicate typical wall peaking profiles that the maxima of the void fraction appeared at the corner made by the heated wall and a side wall. Then, the void fraction decreases gradually as the distance from the heated wall increases. Above the elevation 3.53 m, however, bubbles began to move to the center region of the channel and the void fraction profiles of a core peaking were obtained. The maximum value of the void fraction at a horizontal cross-section appeared at the center of the channel.

Figure 3-(b) shows the experimental results of the local liquid velocity measured with local bi-directional flow tubes. In the measurement, the liquid velocity was positive nearby the heated wall where higher void fraction appeared and negative in the other part. This result shows that the liquid was accelerated by the bubbles resided on the heated wall and then, liquid moved downward in the other region where no bubble existed for the conservation of the mass at the horizontal cross-section. Since the liquid flow rate of the DOBO test is very small, approximately 0.0254 m/s in the cross-sectional average, the natural circulation accelerated by the wall boiling was found to be dominant in the test section. Figure 3-(c) shows the experimental observation result of the downcomer boiling phenomena. Consistent with the experimental measurement results, the bubbles mainly appeared on the heated wall at low elevation, but they began to move toward the center region along the elevation and finally, the flow pattern change from the bubbly flow to the churn flow started at the higher elevation than 4.5 m.

In the experimental result, it was found that the core peaking of the void fraction profile, the flow pattern change from the wall boiling flow to the churn flow and the bubble accelerated natural circulation or the swirling of the liquid are the particular characteristics of the downcomer boiling phenomena. Therefore, the present simulation for the DOBO test was mainly focused on whether these can be reproduced by the CUPID code appropriately.

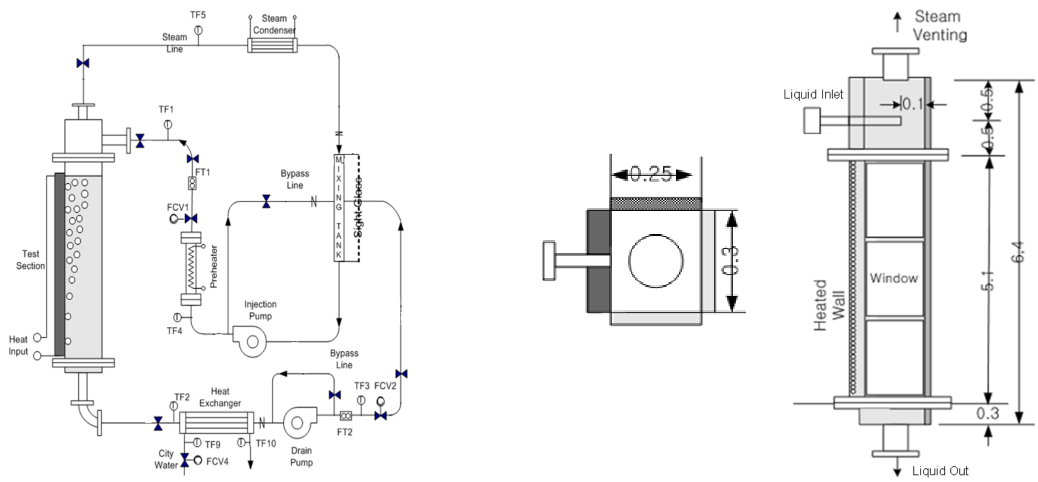

(a) Experimental loop (b) Test section

Figure 2 Schematic diagram of the DOBO facility [27]

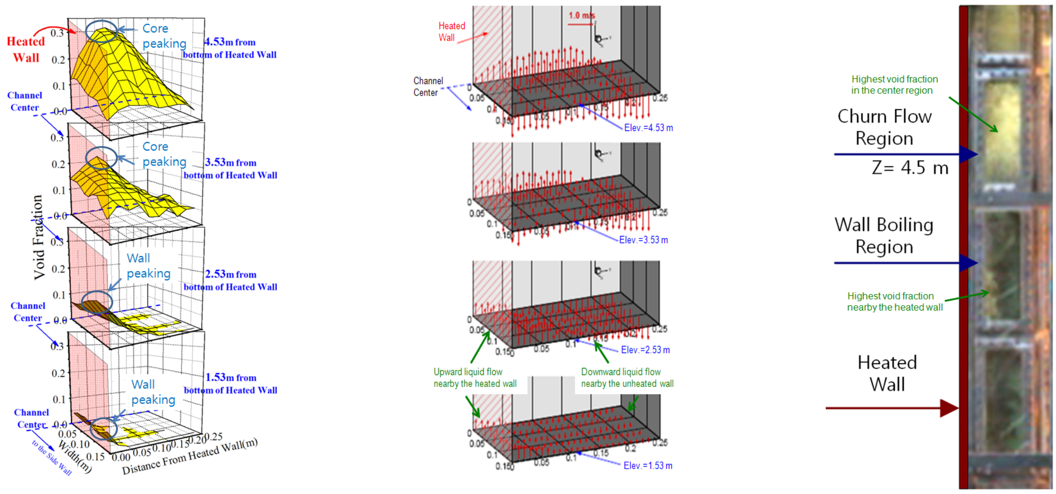

(a) Void fraction (b) Liquid velocity (c) Visual observation

Figure 3 DOBO Experimental Result [27]

4. Two-dimensional simulation result

Figure 4-(a) shows the boundary conditions of the calculation and the computation mesh. The test section was modelled in two-dimensions with the symmetric boundary condition in order to save computational time and to test two-phase flow models conveniently. The experimental results averaged along the depth direction justified this simplification because it showed the overall flow behavior such as the void fraction profile and its transition, the circulation of the liquid flow etc. are well preserved in the averaged quantities. Total 3096 (24×122 for the duct) cells were used for the present calculation. Figure 4-(b) shows the mesh convergence results for void fraction profiles and reasonable convergence was achieved between the default mesh and a finer one in the radial direction (36×122). As same with the experimental procedure, the constant heat flux for the heated wall, the constant pressure for the steam outlet, constant velocity for the liquid inlet conditions were imposed. The liquid outlet flow rate was controlled to maintain the collapsed water level in the test section at 5.4 m.

Figure 5-(a) shows the calculation result of the void fraction with the aforementioned two-phase flow models. The void fraction distributions are compared in Figure 5-(b) at three different elevations (1.53 m, 3.53m and 4.53 m) between the experimental data and the simulation results. At the elevation of 1.53 m (Elevation-1), the wall peaking of the void fraction profiles was obtained in both the experiment and the simulation. Different from the void fraction of the experimental data which showed the monotonous decrease along the x-direction, however, that of the calculation increases for a short distance nearby the heated wall and then decreases gradually. This is mainly considered due to the effect of the large wall lubrication force at the heated wall as shown in Figure 6-(a). The large value of the wall lubrication force is regarded as resulting from the large bubble diameter and further investigations are needed to improve this point. Except this difference, the void fraction profile at Elevation-1 was reasonably well captured by CUPID.

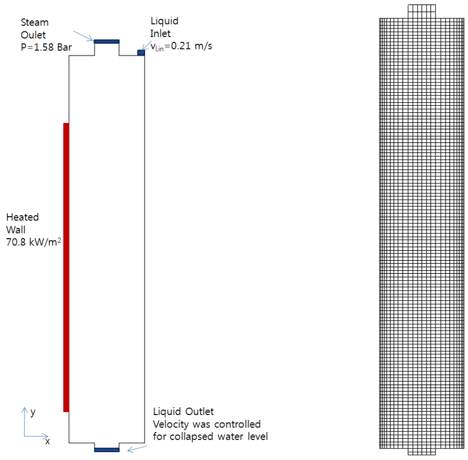

Figure 4-(a) Boundary conditions of the calculation and the computation mesh

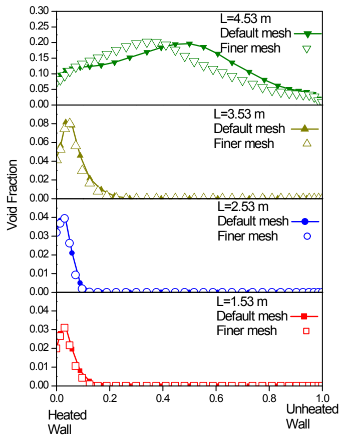

Figure 4-(b) Mesh convergence test result

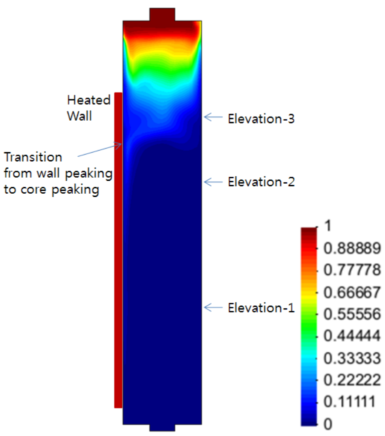

(a) Void fraction distribution

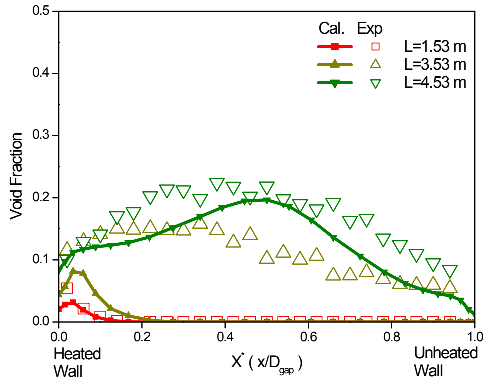

(b) Comparison with the experimental data

Figure 5 CUPID calculation result: void fraction

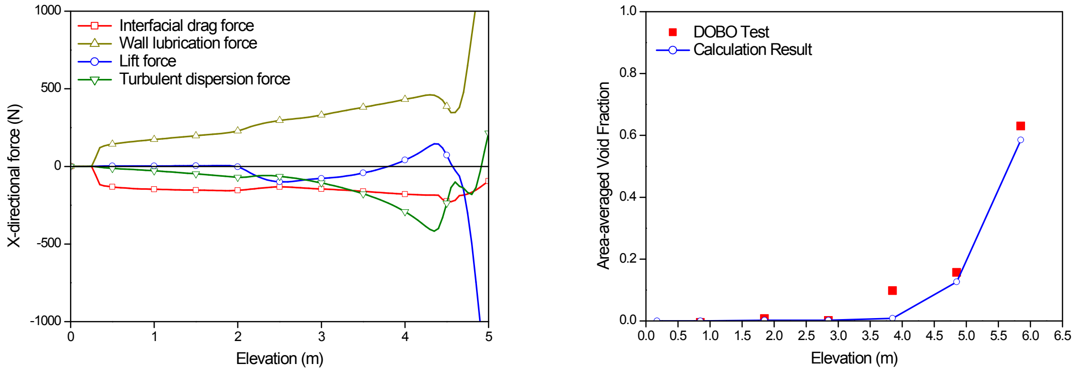

(a) X-directional forces on the heated wall (b) Area averaged void fraction along the elevation

Figure 6 CUPID calculation result

At the elevation of 3.53 m (Elevation-2), a significant difference in void fraction profile was found between the experiment and the calculation. In the experiment, more bubbles were found in the center region of the channel and the core peaking profile of the void fraction was observed. In the calculation, however, the transition from the wall peaking to the core peaking had not yet been started and CUPID predicted a similar profile with that of Eleveation-1. The area-averaged void fraction was under-predicted as well at this elevation as shown in Figure 6-(b). The main reason for this is that the lift force is not strong enough to push the bubbles from the wall. The lift force pushes the bubbles toward the wall if their diameter is smaller than a certain value and vice versa.

The core peaking of the void fraction profile was reasonably well reproduced by the CUPID code at the elevation of 4.53 m (Elevation-3). As shown in Figure 5-(a), the transition from the wall peaking to the core peaking started at approximately 4.2 m and afterwards, the location of the void fraction peak moved to the center of the channel. The predicted bubble diameter increased with void fraction along the elevation and became larger than the criterion for the lift force direction. The lift force became positive value subsequently as shown in Figure 6-(a) and then, started acting toward the central direction. Finally, the peak location of the void fraction begins to move towards the core region when the sum of the lift force and the wall lubrication force is larger than that of the others. Furthermore, as observed in the experiment, the churn flow or annular flow was identified above the Elevation-3 in the calculation, which has a very high void fraction in the core and a very low void fraction on the wall representing a gas core and a liquid film respectively.

This calculation result of the void fraction profile showed that the overall behaviour of the bubbles can be reproduced reasonably by the CUPID code with the present two-phase flow models. However, further improvement of the models is required to enhance the calculation results such as too large value of the wall lubrication force at Elevation-1, under-predicted void fraction at Elevation-2, and the late transition of the wall peaking to core peaking.

Figure 7-(a) indicates the y-directional gas velocities compared between the calculation and the experiment. At Elevation-1 and Elevation-3 where CUPID predicted void fraction profiles correspondent well with the experiment, the gas velocities were reasonably predicted as well. However, at Elevation-2, considerable differences in the predicted gas velocity were found compared to the experiment as in the case of the void fraction. The highest velocities were found at the center of the channel in the experiment while, in the calculation, the maximum velocity was appeared near the wall where the void fraction was high. Figure 7-(b) compares the computational and the experimental results of the y-directional liquid velocities. The circulation of the liquid, the upward flow along the heated wall and the downward flow in the other side, was properly reproduced by the CUPID code. The predicted liquid velocity profile at the wall boiling region (Elevation-1) was in good agreement with the experimental data. In the other elevations, however, it over-predicted the upward velocity and under-predicted the downward one. This implies that the natural circulation of the liquid was accelerated by bubbles excessively in the calculation. This difference seems to be caused by the interfacial drag models and the bubble induced turbulence models. These models will be tested further to improve the calculation of the CUPID code for the downcomer boiling phenomena.

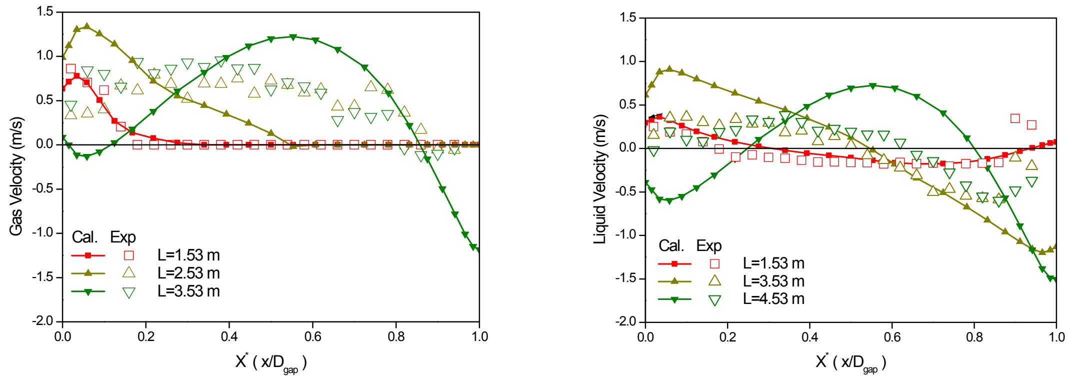

(a) Gas velocity (b) Liquid velocity

Figure 7 CUPID calculation result: y-directional velocities

5. Conclusion

The three-dimensional thermal hydraulics code, CUPID, has been developed for realistic simulation of transient two-phase flows in nuclear reactor components. In the present paper, the physical models and correlations that were employed in the code were introduced and a simulation was performed for the DOBO test facility in order to assess the two-phase flow models. The result showed that it can reproduce the typical characteristics of the downcomer boiling such as the core peaking of the void fraction profile, flow pattern change from the bubbly flow to the churn or annular flow and the bubble accelerated natural circulation of the water. Further improvement in the bubble diameter, the non-drag interfacial forces and the turbulence models is required for an enhanced prediction of the downcomer boiling. The interfacial area transport equation for the bubbly flow region will be tested and the k-ε turbulence model for the churn or annular flow region will be implemented in the future.

Acknowledgments

This work was supported by Nuclear Research & Development Program of the NRF (National Research Foundation of Korea) grant funded by the MEST (Ministry of Education, Science and Technology) of the Korean government (Grant code: M20702040002-08M0204-00210).

Nomenclature

A_i Interfacial area concentration

C Drag coefficient

D Diameter

E_o Eotvos number

f Face

F Interfacial force term

i Cell number

H Interfacial heat transfer coefficient

j Superficial velocity

N Normal vector at a face

Q Interfacial heat transfer term

q Wall heat transfer term

q'' Wall heat flux

S Area of a face at a cell

St Stanton number

V Cell volume

Greek Letter

α Volume fraction

ε Energy dissipation rate per unit mass

χ Interface drag factor

δ Characteristic length

Γ Vapor generation rate

φ Angle

Subscripts

c Continuous phase

k Gas, liquid or droplet

m Mixture

nd Non-drag

ort Orthogonal

τ Tangential

References

[1] C.-H. Song, W. P. Baek, M. K. Chung, and J. K. Park, "Multi-Dimensional Thermal Hydraulic Phenomena in Advanced Nuclear Reactor Systems: Current Status and Perspectives of R&D Program in KAERI," Proc. of NURETH-10, Seoul, Korea, 2003, October 5-9

[2] J.J. Jeong, H.Y. Yoon, I.K. Park and H.K. Cho, "The CUPID Code Development and Assessment Strategy," Nuclear Engineering and Technology, Vol. 42, 2010, pp. 636-655.

[3] H.Y. Yoon, I.K. Park, Y.J. Lee and J.J. Jeong, "An Unstructured SMAC Algorithm for Thermal Non-equilibrium Two-phase Flows," International Communications in Heat and Mass Transfer, Vol. 36, 2009, pp. 16-24.

[4] J.J. Jeong, H.Y. Yoon, I.K. Park, H.K. Cho and H. D. Lee, "Development and Preliminary Assessment of a Three-Dimensional Thermal Hydraulics Code, CUPID," Nuclear Engineering and Technology, Vol. 42, 2010, pp. 279-296.

[5] I.K. Park, H.Y. Yoon, J.J. Jeong, D.J. Euh and H.K. Cho, "An Implementation of the Interfacial Area Transport Equation into the CUPID Code," Proc. of NUTHOS-8, Shanghai, China, 2010, October 10-14.

[6] J.J. Jeong, K.S. Ha, B.D. Chung and W.J. Lee, "Development of a multi-dimensional thermal-hydraulic system code, MARS 1.3.1," Annals of Nuclear Energy, Vol. 26, No. 18, 1999, pp. 1611-1642.

[7] H.G. Joo, J.J. Jeong, B.O. Cho, W.J. Lee and S.Q. Zee, "Analysis of the OECD MSLB benchmark problem using the refined core thermal-hydraulic nodalization feature of the MARS/MASTER code," Nuclear Technology, Vol. 142, 2003, pp. 166-179.

[8] J.R. Lee, H.K. Cho and J.J. Jeong, "Coupled simulation of component thermal hydraulics and neutron kinetics for a nuclear reactor core with CUPID and MASTER," Proc. of KNS Autumn Meeting, Jeju, Korea, 2010, October 21-22.

[9] B.J. Yun, D.J. Euh and C.-H. Song, "Downcomer boiling phenomena during the reflood phase of a large-break LOCA for the APR1400," Nuclear Engineering and Design, Vol. 238, 2008, pp. 2064-2074.

[10] A Tentner et al., "Computational Fluid Dynamics Modeling of Two-Phase Flow in a Boiling Water Reactor Fuel Assembly," Proc. of Mathematics and Computation, Supercomputing, Reactor Physics and Nuclear and Biological Applications, Avignon, France, 2005, September 12-15.

[11] CD-ADAPCO, "STAR-CD Version 4.0 Methodology Manual", Chapter 13, CD-ADAPCO, UK, 2006.

[12] A Tentner et al., "Advances in Computational Fluid Dynamics Modeling of Two-Phase Flow in a Boiling Water Reactor Fuel Assembly," Proc. of ICONE-14, Miami, USA, 2006, July 17-20.

[13] A Tentner et al., "Computational Fluid Dynamics Modeling of Two-Phase Flow Topologies in a Boiling Water Reactor Fuel Assembly," Proc. of ICONE16, Orlando, USA, 2008, May 11-15.

[14] A. Ioilev et al., "Advances in the Modeling of Cladding Heat Transfer and Critical Heat Flux in Boiling Water Reactor Fuel Assemblies," Proc. of NURETH-12, Pittsburgh, USA, 2007, September 30 - October 4.

[15] V. Ustinenko et al., "Validation of CFD-BWR, a New Two-Phase Computational Fluid Dynamics Model for Boiling Water Reactor Analysis," Nuclear Engineering and Design, Vol. 238, 2008, pp. 660-670.

[16] T. Hibiki, T. H. Lee, J. Y. Lee and M. Ishii, "Interfacial area concentration in boiling bubbly flow systems," Chemical Engineering Science, Vol. 61, 2006, pp. 7979-7990.

[17] R. W. Lockhart and R. C. Martinelli, "Proposed correlation of data for isothermal two-phase, two-component flow in pipes," Chemical Engineering Progress, Vol. 5, 1949, pp. 39–48.

[18] I. Kataoka, M. Ishii, and K. Mishima, "Generation and Size Distribution of Droplet in Annular Two-Phase Flow," Trans. ASME, J. Fluid Engineering, Vol. 105, 1983, pp. 230–238.

[19] P. Coste et al., "Status of a Two-phase CFD Approach to the PTS Issue," *XCFD4NRS Workshop*, Grenoble, France (2008).

[20] Ranz and Marshall, "Evaporation from drops: Part I.", Chem. Eng. Prog., Vol. 48, 1952, pp. 141-146.

[21] D. Drew et al., "The analysis of virtual mass effect in two-phase flow," Int. J. Multiphase Flow, Vol 5, 1979, pp. 233-272.

[22] A. Tomiyama, H. Tamia, I. Zun, and S. Hosokawa, "Transverse Migration of Single Bubbles in Simple Shear Flows," Chemical Engineering Science, Vol. 57, 2002, pp. 1849-1858.

[23] S. P. Antal, R T. Lahey, J. E. Flaherty, "Analysis of phase distribution in fully developed laminar bubbly two-phase flow," International Journal of Multiphase Flow, Vol. 7, 1991, pp. 635-652.

[24] J. W. Spore et al., "TRAC-M/FORTRAN 90 (VERSION 3.0) THEORY MANUAL," LA-UR-00-910, Los Alamos National Laboratory, 2000.

[25] B. U. Bae, "Development of CFD Code for Subcooled Boiling Two-Phase Flow with Modeling of the Interfacial Area Transport Equation," Ph.D. Thesis, Seoul National Univ., 2008.

[26] I. Michiyoshi and A. Serizawa, "Turbulence in two-phase bubbly flow," Nuclear Engineering and Design, Vol. 95, 1986, pp. 253-267.

[27] B.J. Yun, A. Splawski, S. Lo and C.-H. Song, "Prediction of a subcooled boiling flow with mechanistic wall boiling and bubble size models," CFD4NRS-3 Workshop, Washington D.C., U.S.A., 2008, September 14-16.